ADVANCED ENERGY MATERIALS
www.advenergymat.de

An Interdigitated Li-Solid Polymer Electrolyte Framework for Interfacial Stable All-Solid-State Batteries

*Yufei Yang, Hao Chen, Jiayu Wan, Rong Xu, Pu Zhang, Wenbo Zhang, Solomon T. Oyakhire, Sang Cheol Kim, David T. Boyle, Yucan Peng, Yinxing Ma, and Yi Cui**

All-solid-state lithium metal batteries are prominent candidates for next-generation batteries with high energy density and low safety risks. However, the traditional planar contact between Li metal and solid-state electrolytes (SSEs) exhibits substantive void formation and large interfacial morphological fluctuation, causing poor interfacial stability. Here, an interdigitated Li-solid polymer electrolyte framework (I-Li@SPE), a pioneering demonstration of 3D interface in polymer-based all-solid-state batteries, is designed, transferring the Li-SSE interfacial contact from planar to 3D for enhanced interfacial integrity. A smooth and intact 3D Li-SSE interfacial contact after repeated cycling that precedes planar Li-SSE contact, is shown. COMSOL simulation indicates I-Li@SPE reduces local current densities by more than 40% and moderates interfacial variation by more than 50%. As a result, I-Li@SPE achieves high critical current density of 1 mA cm^{-2}, as well as promising high areal capacity cycling of 4 mAh cm^{-2} at 0.4 mA cm^{-2}. This work provides a new structure for Li-SSE composite fabrication and high-capacity solid-state Li batteries.

1. Introduction

Lithium metal has been recognized as the most attractive anode candidate for advanced lithium batteries due to its low redox potential (−3.040 V vs standard hydrogen electrode) and high theoretical specific capacity (3860 mAh g^{-1}).[1] However, safety has been a lingering issue for liquid electrolyte batteries. By replacing liquid with solid-state electrolytes (SSEs), all-solid-state Li metal batteries (ASSLMBs) provide a safe and energy-dense battery choice.[2] Still, the practical applications of ASSLMBs have been hindered by Li-SSE interfacial instabilities.[3] Specifically, when Li stripping current density removes Li faster than it can be replenished from the bulk Li electrode, voids form at the Li-SSE interface.[4] This formation and accumulation of voids result in large interfacial resistance and large overpotentials during battery cycling. These large overpotentials reduce the Li reversibility during battery cycling, resulting in quick capacity decay. In addition, the voids and heterogeneities that form at the Li-SSE interface induce high local current densities that result in dendrites growth and short circuit.

To solve the problems associated with the unstable Li-SSE interface, numerous strategies have been deployed, some of which include: 1) interfacial buffer layers for improving Li wettability;[5] 2) MPa to GPa-level external pressure for mechanically deforming Li and reducing void formation;[6] 3) Li metal hosts for improving Li metal plating uniformity.[7] Noticeably, most of the existing strategies are developed based on planar Li-SSE contact. However, this planar contact has two major limitations. The limited contact area between Li and the SSE causes high local current densities during Li stripping and plating. Also, the volume of Li metal varies drastically and primarily along the thickness direction, deteriorating interfacial connection between Li and the SSE. To address the two challenges, it is crucial to make a design transition from planar Li-SSE contact to 3D interfaces. To this end, past reports have shown the promise of 3D Li-SSE interfaces in ceramic solid electrolytes.[8] Besides ceramics, solid polymer electrolytes (SPEs) possessing low interfacial resistance and low density,[9] are prime candidates for 3D Li-SSE demonstrations in ASSLMBs. However, fabrication approaches of 3D Li-ceramics like molten lithium infusion and high-pressure pressing are not adaptable to polymers. Though there are demonstrations of polyethylene glycol (PEG) infusion into Li to construct 3D Li-SPE,[10] the infusion becomes challenging when moving from liquid-state PEG to solid-state polyethylene oxide (PEO). As such, new technical pathways for deploying 3D Li-SPEs for stable ASSLMBs are needed.

Y. Yang, H. Chen, J. Wan, R. Xu, P. Zhang, W. Zhang, S. C. Kim, Y. Peng, Y. Ma, Y. Cui
Department of Materials Science and Engineering
Stanford University
Stanford, CA 94305, USA
E-mail: yicui@stanford.edu
S. T. Oyakhire
Department of Chemical Engineering
Stanford University
Stanford, CA 94305, USA
D. T. Boyle
Department of Chemistry
Stanford University
Stanford, CA 94305, USA
Y. Cui
Stanford Institute for Materials and Energy Sciences
SLAC National Accelerator Laboratory
2575 Sand Hill Road, Menlo Park, CA 94025, USA

The ORCID identification number(s) for the author(s) of this article can be found under https://doi.org/10.1002/aenm.202201160.

DOI: 10.1002/aenm.202201160

In this work, we design an interdigitated Li-SPE (I-Li@SPE) framework to pioneeringly demonstrate 3D interface in polymer-based all-solid-state batteries. This work addresses the challenges of unregulated Li stripping/plating at the planar Li-SPE interface, and significantly improves the interfacial integrity as well as performance of ASSLMBs. The interdigitated Li@SPE design extends Li stripping/plating from a planar Li-SSE interface to 3D, and thus reduces local current densities and suppresses void formation. In addition, I-Li@SPE framework spread the volume change over the much larger 3D interfacial area compared to the 2D planar Li, offering an additional degree of freedom that decreases interfacial fluctuation at the Li-SPE interface. As a result, I-Li@SPE exhibits smoother interface as well as lower interfacial resistance compared to planar Li. The stable interface leads to lower cycling overpotential and longer battery cycle life. In addition, I-Li@SPE design can undertake high current density and high cycling capacity. We demonstrate I-Li@SPE achieves current density (CCD) of 1 mA cm^{-2}, and remarkable high-capacity cycling of 4 mAh cm^{-2} for 100 h at 0.4 mA cm^{-2}. Therefore, our I-Li@SPE electrodes demonstrate a promising design toward practical applications of ASSLMBs.

2. Results and Discussion

Transferring from the planar Li-SPE contact to 3D, our interdigitated Li-SPE framework can effectively improve the interfacial integrity. In planar Li, 2D Li stripping causes relatively high local plating and stripping current densities leading to large interfacial fluctuation.[11] The resulting large interfacial fluctuation causes the aggregation of voids through cycling, leading to high interfacial resistance and dendrite induced shorting (**Figure 1**a). Our design of interdigitated Li-SPE framework (Figure 1b) allows 3D Li stripping and plating that effectively suppresses void formation and interfacial contact fluctuation. As a result, an intact interface is retained after cycling, thereby decreasing overpotential and preventing dendrite-induced shorting. Moreover, with growing capacity, the interfacial fluctuation is exacerbated in planar Li. But in I-Li@SPE, sidewall stripping and plating becomes more pronounced, preventing the deterioration of interface. Thus, the advantages of I-Li@SPE over planar Li become more significant at higher capacity, making I-Li@SPE particularly attractive for high-capacity batteries.

I-Li@SPE can be fabricated within three steps in a roll-to-roll process with upscaling potential (Figure 1c). We use polyethylene hosted polyethylene oxide (PE@PEO) to construct both I-Li@SPE electrodes and SSE, due to its flexibility, thinness, and low cost.[12] PE@PEO is composed through infiltration of PEO based SPE solution into nanoporous PE membrane (Figure S1, Supporting Information). A layer of PE@PEO was first pressed onto a 50 µm thick planar Li foil. Due to the adhesive properties of PE@PEO, it can be easily pressed tightly on Li metal. The combined films were then rolled into a cylindrical shape, and then sliced into round disks. The disk diameter can be easily controlled by the length of the combined films; it can also be reshaped into squares for pouch cell applications through

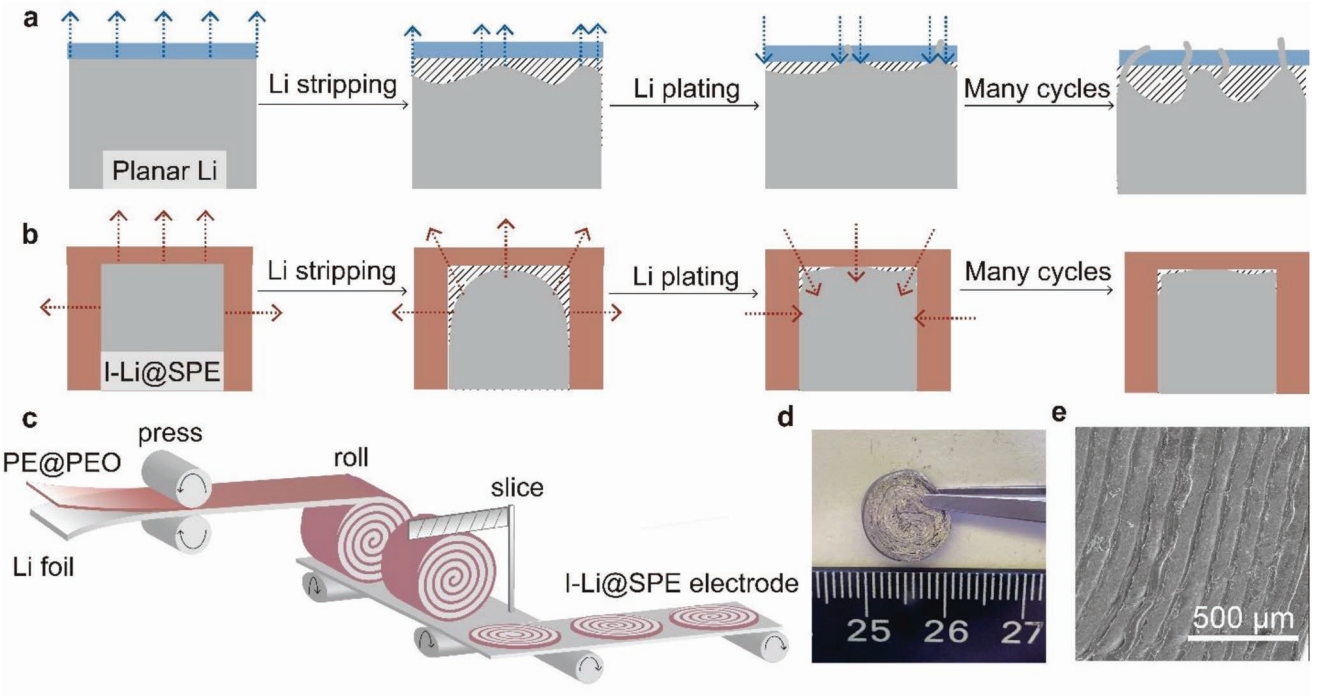

Figure 1. Design and manufacturing of I-Li@SPE electrodes. a) Schematic of Li stripping/plating behavior in planar Li, showing the challenges of high local stripping/platting current densities and huge interfacial fluctuation. Shadow area shows the voids. b) Schematic of stripping/plating behavior in I-Li@SPE, showing promise to maintain the interfacial integrity. c) Schematic for the manufacturing process, which has three major steps: press, roll, and slice. d) Digital photos of I-Li@SPE electrode. e) SEM images of I-Li@SPE, showing the micron-scale roll structure.

remodifying rolling strategies. In this project, the disk diameter is controlled at 3/8 in. (Figure 1d) with thickness around 250 μm (Figure S2, Supporting Information). As shown in Figure 1e, scanning electron microscopy (SEM) further supports the designed alternating blocks of Li and PE@PEO in I-Li@SPE, and demonstrates its smooth surface and closely packed layers. The fabricated I-Li@SPE electrode well remains its interdigitated structure at heated temperature of 60 and 100 °C (Figure S3a, Supporting Information). Furthermore, Li@SPE after repeatable bending and unbending retains its original shape at 100 °C, indicating good mechanical stability even above PEO melting temperature (Figure S3b,c and Video S1, Supporting Information) .

Benefiting from the 3D contact in the I-Li@SPE framework, I-Li@SPE electrode shows significantly enhanced battery performance. As shown in **Figure 2**a, at 60 °C, the critical current density of I-Li@SPE based symmetrical Li–Li cell can reach 1 mA cm^{-2} at a cycling capacity of 0.5 mAh cm^{-2}, while planar Li failed at 0.6 mA cm^{-2}. The doubled critical current density of the I-Li@SPE can be attributed to its reduced local current densities and mitigated interfacial fluctuations. More impressively, we demonstrated symmetric cells cycled at both high current density (0.4 mA cm^{-2}) and high capacity (4 mAh cm^{-2}) (Figure 2b). Planar Li electrode failed in the 1st cycle due to short circuit while I-Li@SPE exhibited stable cycling for more than 100 h. This high-capacity stripping/plating has rarely been demonstrated in ASSLMBs to the best of our knowledge, indicating the prominent future of I-Li@SPE design for high-capacity applications (Figure S4, Supporting Information). Figure 2c further compares the long cycling performance of Li foils and I-Li@SPE symmetric cells at 0.5 mA cm^{-2}, 0.5 mAh cm^{-2}. Planar Li cells showed fluctuating voltage profiles beginning at the initial cycle, indicating severe interface delamination. In comparison, I-Li@SPE electrodes showed constantly smaller overpotentials and stable cycling beyond 200 cycles. Cycling stability of I-Li@SPE also remarkably outperformed planar Li when cycled at 0.3 mA cm^{-2}, 0.3 mAh cm^{-2} (Figure S5a, Supporting Information). Moreover, the symmetric cell cycling performance could be further improved by decreasing the molecular weight of PEO from 3 00 000 to 10 000, by increasing the ionic conductivity (Figure S5b, Supporting Information).

Full cells were fabricated to further evaluate I-Li@SPE electrode performance in practical applications. Lithium iron phosphate (LFP) was chosen as counter electrode. As shown in Figure 2d,e, I-Li@SPE electrodes-based full cell at 60 °C constantly exhibited better rate capability compared to planar Li electrodes-based full cell. In the I-Li@SPE full cell, capacity is retained at 165, 156, 131, 80, 43 mAh g^{-1} at 0.1, 0.2, 0.5, 1, and 2 C rates, while planar Li (P-Li) ‖ LFP cells only offer 148, 138, 97, 37, and 21 mAh g^{-1} at the corresponding C rates. Moreover, I-Li@SPE electrodes outperformed planar Li in the cycling stability (Figure 2f). After 130 cycles at 0.5 C at 60 °C, 99% capacity was retained in I-Li@SPE ‖ LFP cells with capacity of 119 mAh g^{-1}. In contrast, planar Li (P-Li) ‖ LFP cells only exhibits capacity of 48 mAh g^{-1} at 130th cycle, with 40% capacity retention. This performance improvement in both specific capacity and capacity retention suggests that the interfacial stability conferred by the I-Li@SPE is beneficial for long-term cycling of ASSLMBs.

We hypothesize that the stable cycling of I-Li@SPE electrode originates from its improved Li-SSE interfacial integrity. To investigate this hypothesis, we conducted electrochemical impedance spectroscopy (EIS) analysis on Li–Li symmetric cells before cycling and after the 10th, 20th, 30th, and 40th cycle. The corresponding Nyquist plots are shown in **Figure 3**a. The semicircle at the high-frequency range is a good indicator of the interfacial resistance at solid electrolyte interphase (SEI) and the charge transfer resistance at the Li surface.[13] Li foil shows a rapid increase that grew from 114 to 720 Ω (530% increment) within 40 cycles (Figure 3b). In contrast, I-Li@SPE shows a nearly constant interfacial resistance averaged at 108 Ω within 40 cycles, indicating I-Li@SPE retains interfacial integrity during cycling. This improvement can be further supported by the SEM images taken on symmetric cells after 100 cycles (Figure 3c–e). The top-view SEM of the planar-Li design shows large quantity of cracks and protuberance/dendritic structures (Figure 3c) while both the top view (Figure 3d) and side view (Figure 3e) of I-Li@SPE electrodes show a smoother surface without observable dendrites. These results are further supported by the focused-ion-beam SEM conducted on the cycled planar Li and I-Li@SPE electrodes (Figure S6, Supporting Information). The results show that large quantity of voids are accumulated in the planar Li/PEO interface from repeatedly Li stripping/plating, where both the top and side interface of I-Li@SPE electrode show more dense Li morphology. SEI components are also studied by X-ray photoelectron spectroscopy (XPS), showing similar compositions in I-Li@SPE and planar Li interfaces (Figure S7, Supporting Information). This is an expected result since we do not modify the chemical compositions of the interface.

COMSOL simulation further provides theoretical evidence of reduced local current densities and interfacial fluctuations in I-Li@SPE (Figure S8, Supporting Information). **Figure 4**a and Video S2, Supporting Information, show the simulated morphology evolution of I-Li@SPE undergoing 4 mAh cm^{-2} stripping and plating back at 0.1 mA cm^{-2}, displaying 3D Li stripping/plating at both top surface and sidewalls. The edge color represents the local current densities, which is summarized in Figure 4b. The current density at the Li-SPE column is constantly less than 0.1 mA cm^{-2} because large areas of sidewalls disperse the current. More importantly, with the increase of stripping capacity from 1 to 4 mAh cm^{-2}, the current densities on Li top surface decrease ($-22.5\ \mu m < x < 22.5\ \mu m$, see schematics in Figure 4b) while sidewall current densities increase. This result indicates that more Li stripping/plating occurs on sidewalls with increased cycling capacity. SEM was further conducted to disclose the I-Li@SPE morphology to confirm the COMSOL simulation results. The morphological evolution at three states (pristine, stripping 4 mAh cm^{-2}, plating back 4 mAh cm^{-2}) is shown in Figure 4c, and the corresponding top-view SEM images were conducted and shown in Figure 4d. SEM results display evident sidewall stripping and plating, matching the COMSOL simulation results. Additionally, the sidewall stripping and plating mechanism significantly mitigates Li thickness change, which reduces interfacial fluctuation (Figure 4e). Figure 4f summarizes the simulated interfacial thickness fluctuation versus strip capacity in both I-Li@SPE and planar Li, showing a 55% decrease in thickness change of I-Li@SPE compared to planar Li when stripped 2 mAh cm^{-2} away and a 58% reduction when stripped 4 mAh cm^{-2}. Similar improvements are observed in COMSOL simulation results for an I-Li@SPE

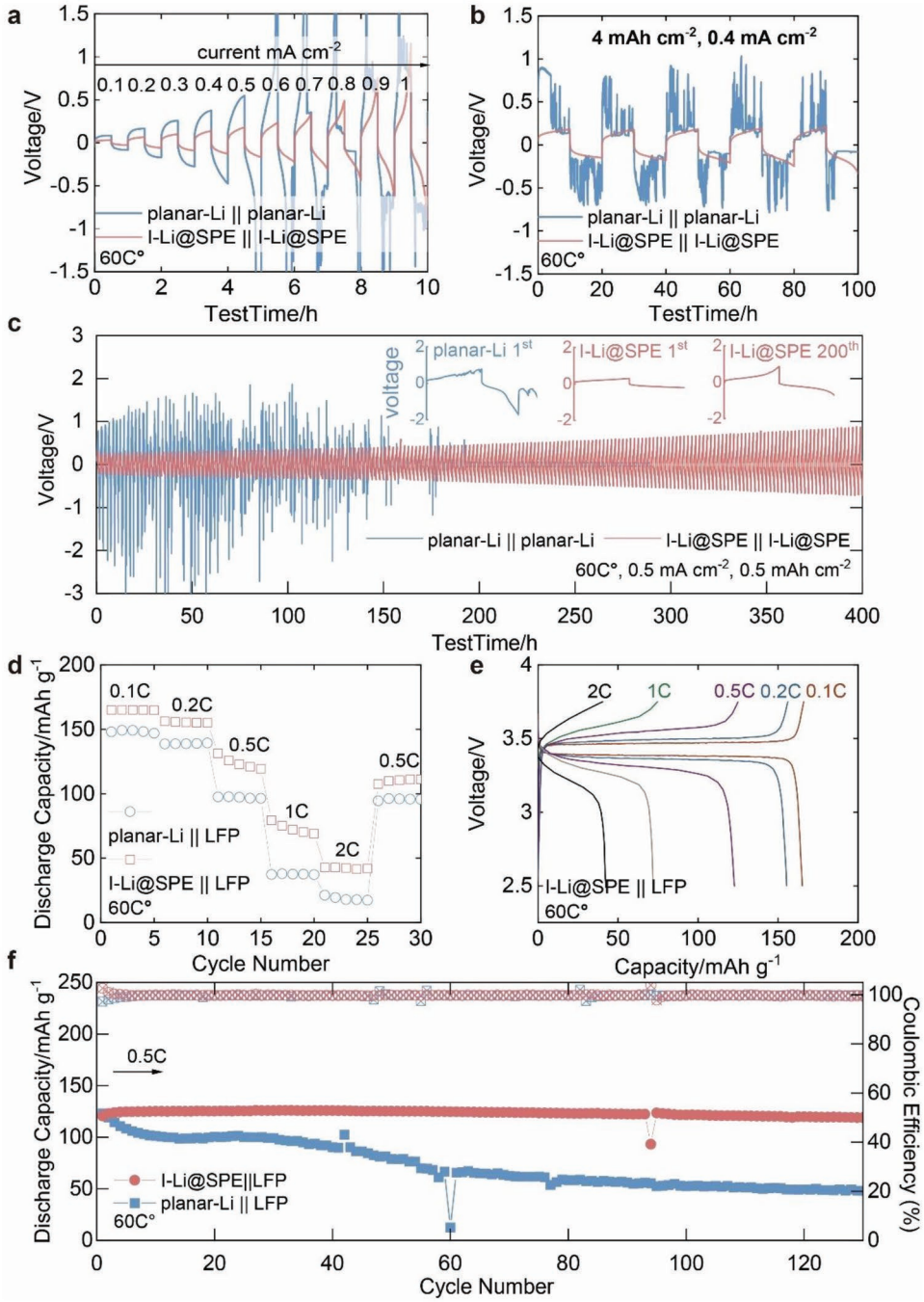

Figure 2. Electrochemical performance of I-Li@SPE electrodes. a) Rate performance of a symmetric I-Li@SPE and planar-Li cell, cycled at different current densities increasing from 0.1 to 1 mA cm^{-2} at 60 °C, 1 h for each cycle. b) Large capacity cycling performance of a symmetric I-Li@SPE and planar-Li cell, cycled at 0.4 mA cm^{-2}, 4 mAh cm^{-2} at 60 °C. c) Long-term cycling of a symmetric I-Li@SPE and planar-Li cell, cycled at 0.5 mA cm^{-2}, 0.5 mAh cm^{-2} at 60 °C. d) Rate performance of I-Li@SPE || LFP and planar-Li || LFP full cell at different charging rates, cycled at 60 °C. e) Voltage profile of I-Li@SPE || LFP full cell, cycled at different charging rates, cycled at 60 °C. f) Cycling performance of a I-Li@SPE || LFP and planar-Li || LFP full cell at 0.5C, cycled at 60 °C.

electrode at a higher current density of 0.4 mA cm^{-2}, verifying the superiority of I-Li@SPE at different current conditions (Figure S9 and Video S3, Supporting Information). These simulations visualize the I-Li@SPE 3D stripping/plating behavior in cycling and provide theoretical support for reduced local current densities and mitigated thickness change in I-Li@SPE.

Additionally, the interfacial evolution of I-Li@SPE/SSE at different stripping/plating states was further investigated through X-ray micro computed tomography (Micro-CT), which non-destructively characterized the 3D morphology of the sample inner structure (Figure S10, Supporting Information).[14] The micro-CT sample was prepared by extracting

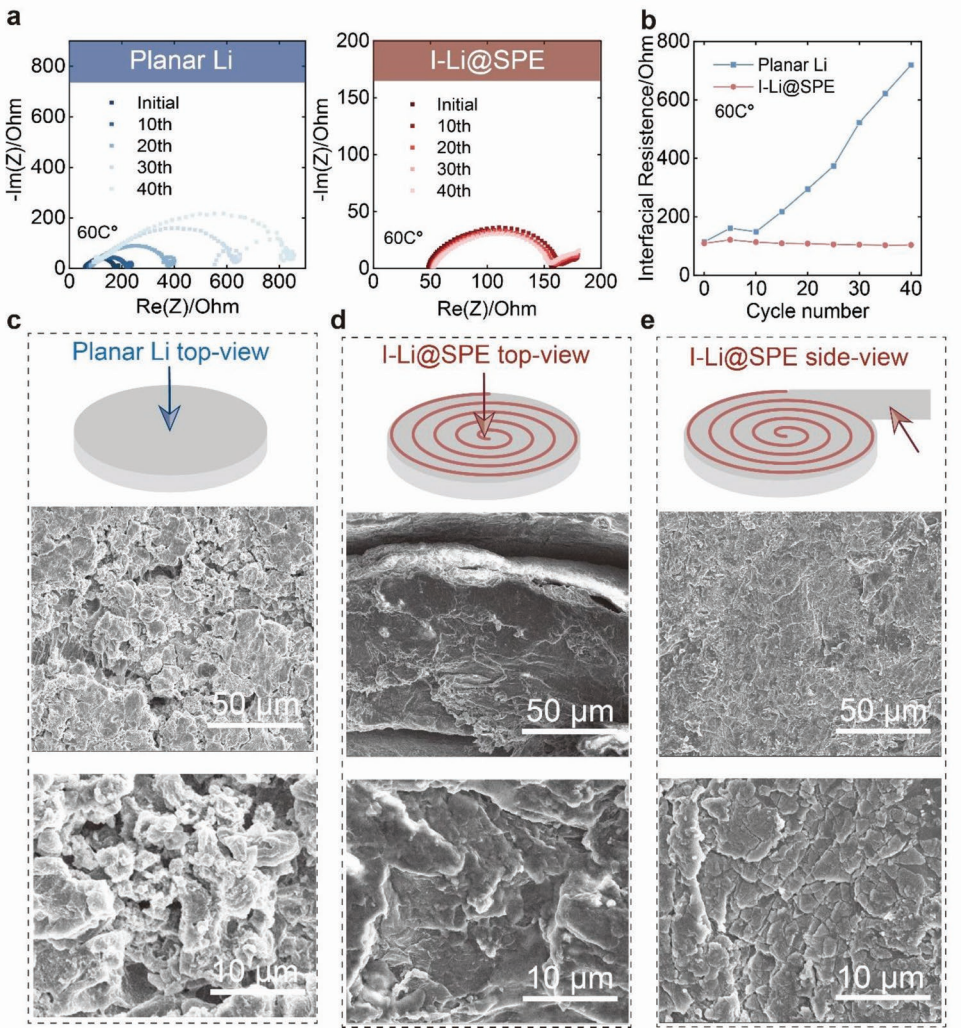

Figure 3. Interfacial properties of I-Li@SPE electrodes. a) Nyquist plots of a symmetric I-Li@SPE cell and a symmetric planar Li cell cycled at 0.3 mA cm^{-2} at 60 °C. b) Interfacial impedance versus cycling number of a symmetric I-Li@SPE cell and a symmetric planar Li cell, cycled at 0.3 mA cm^{-2} at 60 °C. c) SEM images showing the top interface of a planar Li electrode after cycling at 0.3 mA cm^{-2}, 0.3 mAh cm^{-2} at 60 °C for 100 cycles. d–e) SEM images of a I-Li@SPE electrode after cycling at 0.3 mA cm^{-2}, 0.3 mAh cm^{-2} at 60 °C for 100 cycles: d) top interface and e) side interface.

a millimeter-scale cube from the I-Li@SPE/SSE/Li bulk (**Figure 5**a). The sample was rotated through 180° while capturing radiographic projections which were subsequently reconstructed in 3D. The reconstructed 3D morphologies were collected at two different states: stripping 4 mAh cm^{-2} from I-Li@SPE, and plating back 4 mAh cm^{-2} in I-Li@SPE (Figure 5b,c), revealing the retained interdigitated structure in I-Li@SPE throughout the stripping/plating cycle. Furthermore, Figure 5d,e shows the amplified interface at stripping and plating back states, respectively. After stripping 4 mAh cm^{-2} Li away, a medium greyscale appears at the interface. Because X-ray imaging contrast is highly dependent on density,[15] this medium greyscale region indicates a region other than Li metal and SPE, which is likely to be a poor contact region filled with holes and SPE at the interface. Importantly, the intermediate region is recovered after plating back 4 mAh cm^{-2} Li. This phenomenon suggests the recovery of intact Li-SSE interface after Li stripping/platting cycles, which is also supported by the previous SEM and COMSOL simulation results.

3. Conclusion

To address the interfacial challenges in all-solid-state Li batteries, we design an interdigitated Li metal-SPE framework to construct 3D contact between Li and SSE. Through roll-to-roll fabrication, we address the fabrication difficulty of Li-SPE composite and provide new insights for composite electrode design. This interdigitated Li-SPE framework effectively reduces local stripping and plating current densities and mitigates interfacial fluctuation. Consequently, the I-Li@SPE design exhibits stable interfacial resistance during cycling. Using SEM, we present a smooth Li surface without dendrites after 100 cycles, and using micro-CT, we reveal an intact Li-SSE interface after 4 mAh cm^{-2} of stripping and plating in the I-Li@SPE cells. We further demonstrate that I-Li@SPE exhibits good battery performance, particularly at high current density and cycling capacity, revealing the potential of this 3D framework for practical high-capacity batteries. In summary, our interdigitated Li-SSE framework provides a promising

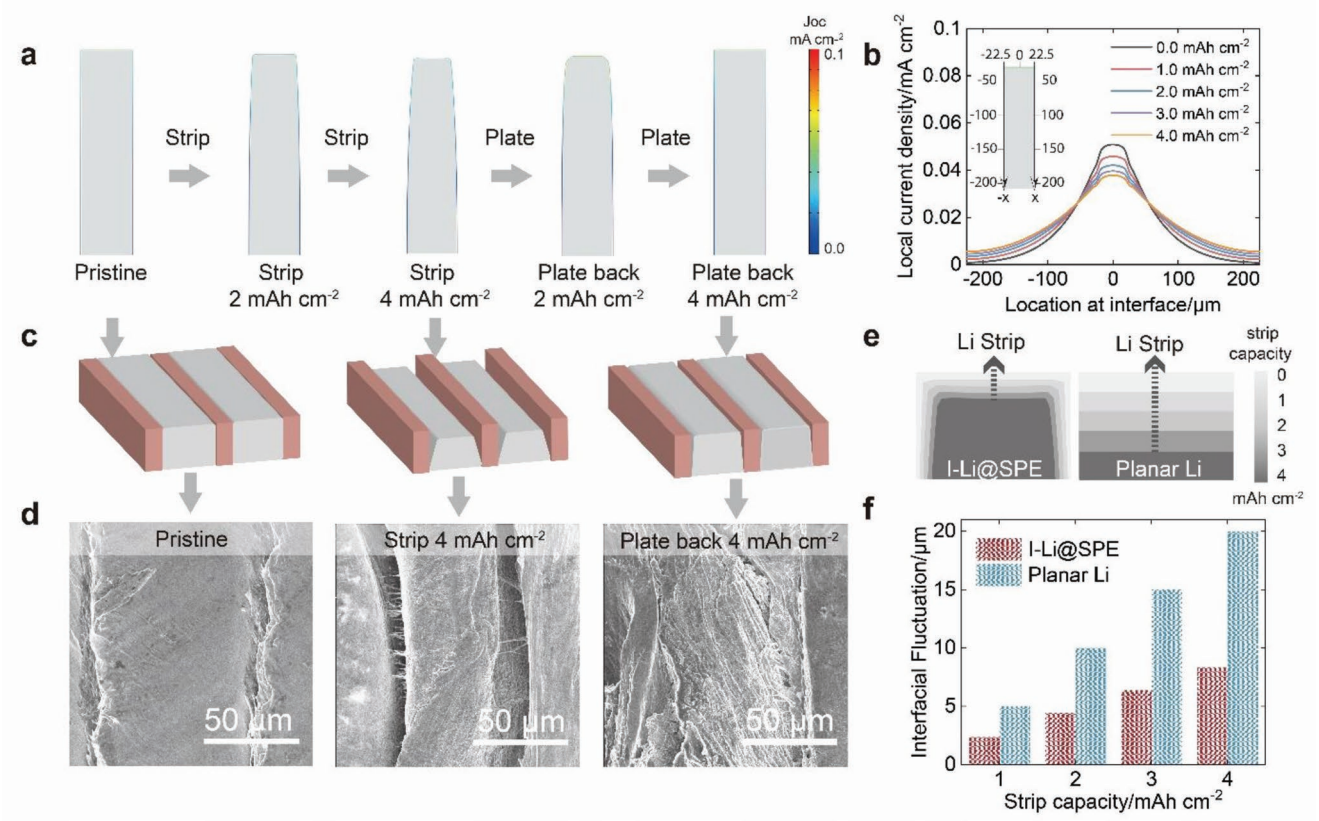

Figure 4. COMSOL Multiphysics modeling of I-Li@SPE electrodes in stripping/plating. a) The COMSOL simulation result of the morphology evolution of a I-Li@SPE electrode in a stripping 4 mAh cm^{-2} and then plating back 4 mAh cm^{-2} process. The current for stripping was limited at 0.1 mA cm^{-2}. b) The COMSOL simulation result of the evolution of the local current density distribution on the I-Li@SPE column with increased stripping capacity. c) Schematic of the I-Li@SPE electrode at the pristine state and after stripping 4 mAh cm^{-2}, and after plating back 4 mAh cm^{-2}, respectively. d) Corresponding top-view SEM images of the I-Li@SPE electrode at the initial state and after stripping 4 mAh cm^{-2}, and after plating back 4 mAh cm^{-2}, respectively. e) The COMSOL simulation result of the interfacial evolution of I-Li@SPE and planar Li with increased stripping capacity. f) The COMSOL simulation result of interfacial fluctuation thickness versus strip capacity of I-Li@SPE and planar Li electrodes.

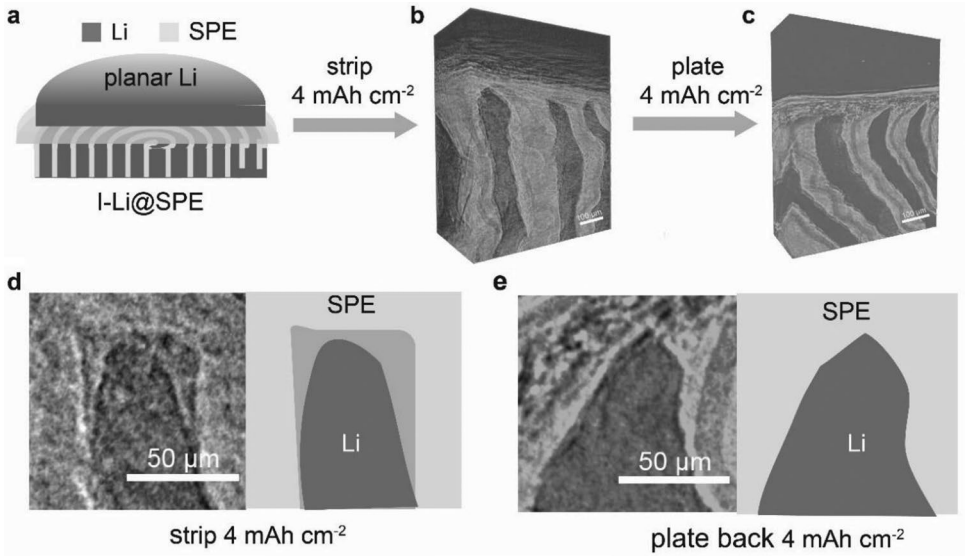

Figure 5. Micro-CT characterization of I-Li@SPE electrodes. a) Schematic of the sample prepared for micro-CT characterization. The 3D-reconstructed photographs b) of the sample after stripping 4 mAh cm^{-2} from I-Li@SPE and c) the sample after plating back 4 mAh cm^{-2} in I-Li@SPE. The black region represents Li metal, and the white region represents solid polymer electrolyte. The corresponding amplified 2D images of d) the sample after stripping 4 mAh cm^{-2} from I-Li@SPE and e) the sample after plating back 4 mAh cm^{-2} in I-Li@SPE.

design principle and offers insights for next-generation high-energy solid-state Li batteries.

4. Experimental Section

Preparation of Solid-State Electrolyte PE@PEO: Polyethylene oxide filled polyethylene (PE@PEO) was chosen as the SSE to demonstrate the paper idea. PEO (MW = 3 00 000, Sigma-Aldrich) was mixed with LiTFSI (Solvay) and acetonitrile (anhydrous, Sigma-Aldrich) using a Thinky mixer (Thinky Cooperation). The EO to Li ratio was 10:1. As-prepared PEO/LiTFSI/acetonitrile solution was blade casted onto a porous PE film (Entek, 12 µm thick), followed by drying in a vacuum oven at 60 °C for 24 h. The vacuum environment ensured the filtration of PEO/LiTFSI into the nanopores of the PE. The obtained PE@PEO film was stored in an Ar-filled glovebox for future use.

Preparation of I-Li@SPE Composite: In an Ar-filled glovebox, a piece of Li foil (Hydro-Quebec, 50 µm thick) was hot pressed at 60 °C onto a piece of PE@PEO film with the same dimension. The viscous PEO at 60 °C makes two films easily adhere together. Then the composite was rolled up to produce an I-Li@SPE composite scroll, followed by inserting into a PTFE tube (diameter 3/8 in.) to normalize the cross-section area at ≈0.7 cm^2. The composite was heated at 60 °C overnight, when the viscous PEO and the tube pressure compress the roll into a tightly bound scroll. The I-Li@SPE scroll was then cut into small disks with the thickness of ≈250 µm by a razor blade. This thickness was obtained through simple sharp blade cutting, which can be further reduced by more advanced slicing techniques. The round I-Li@SPE disk may experience some shape deformation during the cutting process, but the cross-section area will be kept at ≈0.7 cm^2. The PTFE ring was taken out after cutting.

Electrochemical Characterizations: Symmetric cells and full cells were made to test the I-Li@SPE electrochemical performance. All cells were set up in 2032 type coin cells and tested inside an environmental chamber (BTU-133, ESPEC North America) at 60 °C. For symmetric cells, a symmetric structure of I-Li@SPE/PE@PEO/I-Li@SPE was constructed. For full cells, lithium ion phosphate (LFP) was used as the cathode electrode, which was prepared by mixing LFP powders (MTI), PEO/LiTFSI, and carbon black (w:w:w = 60:25:15) in acetonitrile using a Thinky mixer. The slurry was then bladed onto Al foil, followed by drying in vacuum oven at 60 °C for at least 48 h. The LFP active material loading was 2.5–3.5 mg cm^{-2}. Built-up cells were loaded into LAND system for rate and cycling performance test and Bio-logic VMP3 for EIS measurement. Batteries were activated at 0.05 mA cm^{-2} (symmetric cells) or 0.1C (full cells) for five cycles before measurement. Pure Li metal (0.75 mm thick, Alfa Aesar) was used as the control of I-Li@SPE.

Material Characterizations: SEM images were taken with an FEI Mcagellan 400 XHR scanning electron microscope at an acceleration voltage of 5 kV and a 4 mm working distance. Focused ion beam SEM images were taken with FEI Helios NanoLab 600i DualBeam focused-ion-beam/SEM. Samples were cross-sectioned with a Ga^+ ion beam. Before SEM characterization, batteries were disassembled in an Ar-filled glovebox, and PE@PEO film was gently peeled off from I-Li@SPE electrode to reveal the I-Li@SPE-SSE interface. XPS was collected with PHI VersaProbe 3 XPS probe with an Al K-alpha source. The air-sensitive lithium sample was transferred from the Ar glovebox to the XPS measurement station in a vacuum transfer vessel to prevent any air exposure at all times. The binding energies were calibrated with respect to the C 1s peak at 284.8 eV.

Micro-CT was taken with a lab-based X-ray micro-CT instrument (Zeiss Xradia 520 Versa, Carl Zeiss Inc., CA, USA). The instrument with a polychromatic micro-focus sealed source was set to an accelerating voltage of 80 kV on a tungsten target and a maximum power of 7 W. The scintillator was coupled to a 20× objective lens. The 2048 × 2048 pixel CCD detector was set with a pixel binning of 2, which results in a pixel size of ≈0.81 µm and a field of view of ≈803 µm for the 20× objective. Samples were prepared by extracting a millimeter-scale cube from the I-Li@SPE/SSE/Li bulk followed by sealing in a close-end polyimide tube for air isolation. The tube containing I-Li@SPE||SSE||Li was rotated 360° and 3500–4500 radiographs were collected at angular intervals at an exposure time of 2–2.5 s (detailed parameters are listed in Table S1, Supporting Information). Since samples were set close to detector, there was no significant geometric magnification as the effects of penumbral blurring was minimized. The projection dataset was reconstructed into a 3D volume in the Zeiss XMReconstructor software (Carl Zeiss Inc.) implemented with modified Feldkamp–David–Kress (FDK) algorithm for cone beam geometry. The further 3D analysis was carried out in Dragonfly Pro software for filtering and segmentation.

COMSOL simulation: A numerical model to better understand the coupled electrochemical behavior and morphological evolution of I-Li@SPE electrode during Li stripping/plating, was developed. The Li ion transport in polymer electrolyte and the charge transfer reactions at Li/SSE interfaces were described by the Nernst–Planck equation and the Butler–Volmer equation, respectively, and numerically solved by the electrochemical module integrated in COMSOL Multiphysics software. The deformation of Li electrodes caused by Li deposition of dissolution was simulated by the deformed geometry module in COMSOL that had been coupled with the electrochemical module. To simulate the increase of resistance at the Li/SSE interface due to local detachment, an interfacial resistance layer between Li and electrolyte, was added. The resistance R_{int} is determined by a power-law relation to the interfacial gap, $R_{int} = A \cdot l^B$, where A and B are fitted parameters, and l (µm) is the interfacial gap between Li and electrolyte. Details of the electrochemical model are included in Note S1, Supporting Information. The geometrical and electrochemical parameters in the numerical model were set to be consistent with the experimental setup. The galvanostatic cycling was simulated by applying a constant current density (0.1 or 0.4 mA cm^{-2}) on the Li metal electrode. Related physical properties of Li metal and polymer electrolyte are listed in Table S2, Supporting Information.

Supporting Information

Supporting Information is available from the Wiley Online Library or from the author.

Acknowledgements

Y.Y., H.C., and J.W. contributed equally to this work. Part of this work was performed at the Stanford Nano Shared Facilities and Stanford Nanofabrication Facility. This work was partially supported by the Assistant Secretary for Energy Efficiency and Renewable Energy, Office of Vehicle Technologies of the U.S. Department of Energy under the Battery Materials Research program and the Battery500 Consortium program. Robyn Brinks Lockwood from Stanford University kindly helped with language editing for this article.

Conflict of Interest

The authors declare no conflict of interest.

Data Availability Statement

The data that support the findings of this study are available from the corresponding author upon reasonable request.

Keywords

3D interfaces, all-solid-state batteries, Li metal batteries, solid polymer electrolytes

Received: April 4, 2022
Revised: July 21, 2022
Published online:

[1] a) D. Lin, Y. Liu, Z. Liang, H.-W. Lee, J. Sun, H. Wang, K. Yan, J. Xie, Y. Cui, *Nat. Nanotechnol.* **2016**, *11*, 626; b) D. Lin, Y. Liu, Y. Cui, *Nat. Nanotechnol.* **2017**, *12*, 194; c) X.-B. Cheng, R. Zhang, C.-Z. Zhao, Q. Zhang, *Chem. Rev.* **2017**, *117*, 10403; d) H. Chen, A. Pei, J. Wan, D. Lin, R. Vilá, H. Wang, D. Mackanic, H.-G. Steinrück, W. Huang, Y. Li, *Joule* **2020**, *4*, 938.

[2] a) Q. Zhao, S. Stalin, C.-Z. Zhao, L. A. Archer, *Nat. Rev. Mater.* **2020**, *5*, 229; b) J. Janek, W. G. Zeier, *Nat. Energy* **2016**, *1*, 16141; c) J. Wan, J. Xie, X. Kong, Z. Liu, K. Liu, F. Shi, A. Pei, H. Chen, W. Chen, J. Chen, *Nat. Nanotechnol.* **2019**, *14*, 705.

[3] K. B. Hatzell, X. C. Chen, C. L. Cobb, N. P. Dasgupta, M. B. Dixit, L. E. Marbella, M. T. McDowell, P. P. Mukherjee, A. Verma, V. Viswanathan, *ACS Energy Lett.* **2020**, *5*, 922.

[4] a) C. Monroe, J. Newman, *J. Electrochem. Soc.* **2005**, *152*, A396; b) J. Kasemchainan, S. Zekoll, D. S. Jolly, Z. Ning, G. O. Hartley, J. Marrow, P. G. Bruce, *Nat. Mater.* **2019**, *18*, 1105; c) T. Krauskopf, H. Hartmann, W. G. Zeier, J. Janek, *ACS Appl. Mater. Interfaces* **2019**, *11*, 14463.

[5] a) X. Han, Y. Gong, K. K. Fu, X. He, G. T. Hitz, J. Dai, A. Pearse, B. Liu, H. Wang, G. Rubloff, *Nat. Mater.* **2017**, *16*, 572; b) W. Luo, Y. Gong, Y. Zhu, K. K. Fu, J. Dai, S. D. Lacey, C. Wang, B. Liu, X. Han, Y. Mo, *J. Am. Chem. Soc.* **2016**, *138*, 12258; c) C. Wang, H. Xie, L. Zhang, Y. Gong, G. Pastel, J. Dai, B. Liu, E. D. Wachsman, L. Hu, *Adv. Energy Mater.* **2018**, *8*, 1701963.

[6] a) M. J. Wang, R. Choudhury, J. Sakamoto, *Joule* **2019**, *3*, 2165; b) X. Zhang, Q. J. Wang, K. L. Harrison, K. Jungjohann, B. L. Boyce, S. A. Roberts, P. M. Attia, S. J. Harris, *J. Electrochem. Soc.* **2019**, *166*, A3639; c) Y. Qi, C. Ban, S. J. Harris, *Joule* **2020**, *4*, 2599.

[7] a) S.-S. Chi, Y. Liu, N. Zhao, X. Guo, C.-W. Nan, L.-Z. Fan, *Energy Storage Mater.* **2019**, *17*, 309; b) X. Yang, X. Gao, C. Zhao, Q. Sun, Y. Zhao, K. Adair, J. Luo, X. Lin, J. Liang, H. Huang, *Energy Storage Mater.* **2020**, *27*, 198.

[8] a) C. Yang, L. Zhang, B. Liu, S. Xu, T. Hamann, D. McOwen, J. Dai, W. Luo, Y. Gong, E. D. Wachsman, *Proc. Natl. Acad. Sci. USA* **2018**, *115*, 3770; b) R. Xu, F. Liu, Y. Ye, H. Chen, R. R. Yang, Y. Ma, W. Huang, J. Wan, Y. Cui, *Adv. Mater.* **2021**, *33*, 2104009; c) C. Wang, Y. Gong, B. Liu, K. Fu, Y. Yao, E. Hitz, Y. Li, J. Dai, S. Xu, W. Luo, *Nano Lett.* **2017**, *17*, 565.

[9] a) Y. Cui, J. Wan, Y. Ye, K. Liu, L.-Y. Chou, Y. Cui, *Nano Lett.* **2020**, *20*, 1686; b) T. F. Miller III, Z.-G. Wang, G. W. Coates, N. P. Balsara, *Acc. Chem. Res.* **2017**, *50*, 590.

[10] a) Y. Liu, D. Lin, Y. Jin, K. Liu, X. Tao, Q. Zhang, X. Zhang, Y. Cui, *Sci. Adv.* **2017**, *3*, eaao0713; b) X. Gao, X. Yang, K. Adair, J. Liang, Q. Sun, Y. Zhao, R. Li, T. K. Sham, X. Sun, *Adv. Funct. Mater.* **2020**, *30*, 2005357.

[11] D. Cao, X. Sun, Q. Li, A. Natan, P. Xiang, H. Zhu, *Matter* **2020**, *3*, 57.

[12] a) Y. Ma, J. Wan, Y. Yang, Y. Ye, X. Xiao, D. T. Boyle, W. Burke, Z. Huang, H. Chen, Y. Cui, *Adv. Energy Mater.* **2022**, *12*, 2103720; b) J. Wu, Z. Rao, Z. Cheng, L. Yuan, Z. Li, Y. Huang, *Adv. Energy Mater.* **2019**, *9*, 1902767.

[13] G. Bieker, M. Winter, P. Bieker, *Phys. Chem. Chem. Phys.* **2015**, *17*, 8670.

[14] a) M. Feser, J. Gelb, H. Chang, H. Cui, F. Duewer, S. Lau, A. Tkachuk, W. Yun, *Meas. Sci. Technol.* **2008**, *19*, 094001; b) S. Hao, J. J. Bailey, F. Iacoviello, J. Bu, P. S. Grant, D. J. Brett, P. R. Shearing, *Adv. Funct. Mater.* **2021**, *31*, 2007564.

[15] J. Tippens, J. C. Miers, A. Afshar, J. A. Lewis, F. J. Q. Cortes, H. Qiao, T. S. Marchese, C. V. Di Leo, C. Saldana, M. T. McDowell, *ACS Energy Lett.* **2019**, *4*, 1475.